

# MODELING OF FAR-FIELD QUANTUM COHERENCE BY DIELECTRIC BODIES BASED ON THE VOLUME INTEGRAL EQUATION METHOD

Chengnian Huang<sup>1</sup>, Hangyu Ge<sup>1</sup>, Yijia Cheng<sup>1</sup>, Zi He<sup>2</sup>, Feng Liu<sup>1</sup> and Wei E. I. Sha<sup>1,\*</sup>

<sup>1</sup> College of Information Science and Electronic Engineering, Zhejiang University, Hangzhou 310027, China.

<sup>2</sup> Department of Communication Engineering, Nanjing University of Science and Technology, Nanjing 210094, China.

Correspondence: weisha@zju.edu.cn

## ABSTRACT

The Hong–Ou–Mandel (HOM) effect is a hallmark of nonclassical photon interference. Accurate modeling of angle-resolved two-photon correlations in complex dielectric structures remains challenging due to the lack of an efficient numerical framework that directly connects classical electromagnetic quantities with quantum correlation functions. This study establishes a unified theoretical and computational framework to evaluate far-field HOM interference patterns from arbitrary dielectric bodies. By quantizing the plane-wave scattering modes and computing their far-field responses via the volume integral equation (VIE) method, the second-order normalized correlation function is determined without resorting to near-to-far field transformations or perfectly matched layers. This enables efficient evaluation of both frequency-domain correlations and time-domain coincidence counts for photon wave packets. The method is validated against analytical solutions for dielectric spheres and further applied to a polarization-converting Pancharatnam–Berry-phase (PBP) metasurface, revealing strong angular dependence of quantum interference that is directly correlated with the characteristics of the HOM dip. The results demonstrate that the proposed framework provides a computationally efficient and physically transparent tool for exploring structure-dependent quantum correlations, with potential applications in quantum antennas, metasurface-based quantum state engineering, and quantum inverse design.

**Keywords** Hong-Ou-Mandel (HOM) effect · volume integral equation (VIE) method · far-field interference · correlation function · coincidence counts

## 1 Introduction

Over the past few years, the quantum information[1, 2], quantum computing[3], quantum optics[4], and related photonic quantum technologies have achieved remarkable progress, which also propelled the advancement of corresponding theoretical and numerical methods. Owing to the intriguing characteristics of quantum optics, extensive studies including spontaneous emissions rates[5, 6, 7] in dielectric media [8], Casimir forces[9], artificial atoms[10], few-photon interference in passive and lossless quantum-optical instruments[11], quantum-optical metamaterials[12], etc, have been conducted based on the macroscopic quantum electrodynamics theory[13, 14]. The extension of relevant concepts inspired the versatile applications of microwave photons in realistic quantum optical elements and systems such as quantum radars[15, 16, 17], quantum antennas[18], beam splitters[4, 19, 20], and different types of interferometers[21]. In this process, the wave scattering exhibits non-classical behaviors due to its possibility of controlling the quantum statistics of photon at the frequency domain[22]. When a single photon undergoes scattering, its multiple paths give rise to an interference pattern identical to that observed for a classical wave at the same optical mode. While two or more photons scatter, interference of the photons occupied by the Fock states[23, 24, 25] induces the quantum correlation, which is distinct from the classical scattering[26]. This behavior is exemplified by the Hong-Ou-Mandel (HOM) effect[27, 28] referring to the suppression of coincidence counts due to two-photon interference in a 50/50 quantum beam splitter. It provides compelling evidence for the non-classical behavior of entangled photons, reflecting both the quantized nature of the electromagnetic fields and the indivisibility of individual photons.

In order to elucidate the quantum nature of electromagnetic fields underlying these observations, a wide range of analytic and numerical methods have been employed in quantum optics. Quantization schemes based on variable separation have been proposed in [29] and [30] to solve the spherically layered multimode systems and parabolic mirrors, an analytical approach in [31] is employed to calculate the far-field correlation function of a dielectric sphere. And the ubiquitous Green's function method is widely used in many quantum calculations[32, 33, 34]. Considering the arbitrary lossless quantum-optical systems for inhomogeneous dielectric media, the reformulation of the quantum Maxwell's equations frequently relies on constructing the numerical normal modes. By replacing the classical expansion coefficients with creation and annihilation operators, quantum information is injected into the modal basis, thereby enabling the manifestation of quantum effects[4, 19, 35, 36]. In [13, 37, 38], computational electromagnetic (CEM) techniques like the finite-difference (FDM)[39], finite-element method (FEM)[40] and finite-difference time-domain (FDTD) method[41] are utilized to directly solve the normal modes of Helmholtz wave equations. Alternatively, [22] adopts the method of characteristic modes[42, 43, 44, 45, 46, 47] to calculate the principal modes of the perfectly conducting body, which are particularly appropriate for analyzing the scattering-induced entanglement because of their orthogonality and physical distinguishability. While the superposition of multiple quantized modes provides a complete and rigorous representation of electromagnetic fields, in the far-field regime, the modes at different angular directions can be approximated as mutually orthogonal and complete plane-wave components. Under these conditions, frequency-domain formulations enable efficient analysis of far-field interference effects from complex dielectric structures. Building on the theoretical framework in [48], photodetection correlation functions are expressed in terms of the local and cross densities of states of the classical electromagnetic fields. By computing the far-field polarization components of independently incident single-photon beams in the frequency domain, the angle-dependent two-photon interference phenomena characterized by HOM features can be analyzed in the far-field regime.

In this paper, we investigate the far-field interference properties of two-photon scattering on dielectric structures via the volume integral equation (VIE) method. A framework for the second-order normalized correlation function is established, assuming each photon occupies a normalized scattering eigenmode at the frequency domain. Moreover, the normalized coincidence number as a function of time delay can also be derived by evaluating the far-field response at specific eigenmodes. For each mode excitation, the VIE method is employed to compute the corresponding polarization currents, which allow for the direct far-field evaluation and eliminate the need for the near-to-far field transformations or perfectly matched layers (PMLs) commonly required in differential numerical methods. Additionally, the preconditioner and fast algorithm like fast Fourier transform (FFT) could be combined with the VIE method to accelerate the simulation of the large-scale dielectric nanostructures[49].

The main contributions of this work are summarized as follows: 1. We develop a unified framework based on the VIE and dyadic Green's function, which directly links classical far-field scattering to quantum second-order correlation functions. 2. The proposed approach avoids the heavy modal expansion and convergence issues of conventional quantum FDTD or normal-mode methods, thus achieving higher efficiency and numerical stability. 3. We seamlessly connect the frequency-domain correlation functions with time-domain coincidence measurements, enabling faithful reproduction of experimentally observable HOM interference phenomena.

The paper is outlined as follows: In Sec. II, we introduce the fundamental concepts of the quantum electromagnetic fields, together with the derivation of the correlation function in the frequency domain and the normalized coincidence number function in the time domain. In Sec. III, we consider two examples of two-photon interference effects on the dielectric sphere and the polarization-converting metasurface. Sec IV concludes the paper with a summary and an outlook on future development.

## 2 Theory

In the classic world, the observable physical quantity such as position or velocity is deterministic. However, in view of the intrinsic quantum fluctuations, the state of a photon has to be endowed by a wave function  $|\Psi\rangle$  in the microscopic regime. Given a non-entangled single photon in the form of a wave packet[50], the corresponding state in the Heisenberg picture can be expressed as a coherent superposition of multimode Fock states

$$|\Psi\rangle = \sum_{n=1}^N \phi_n |1\rangle_n = \sum_{n=1}^N \phi_n \hat{a}_n^\dagger |0\rangle \quad (1)$$

where  $\phi_n$  denotes the probability amplitude of the Fock state  $|1\rangle_n$ , incorporating the spectral profile of the wave packet;  $\hat{a}_n^\dagger$  is the creation operator, and  $|0\rangle$  denotes the vacuum state. If the two photons are non-entangled, the initial quantum state of the ensemble can be expressed as the tensor product, namely:  $|\Psi\rangle_{12} = |\Psi\rangle_1 \otimes |\Psi\rangle_2$ . Similarly, the classical field quantities in Maxwell's equations are elevated to the field operators in the quantum formalism. The general field

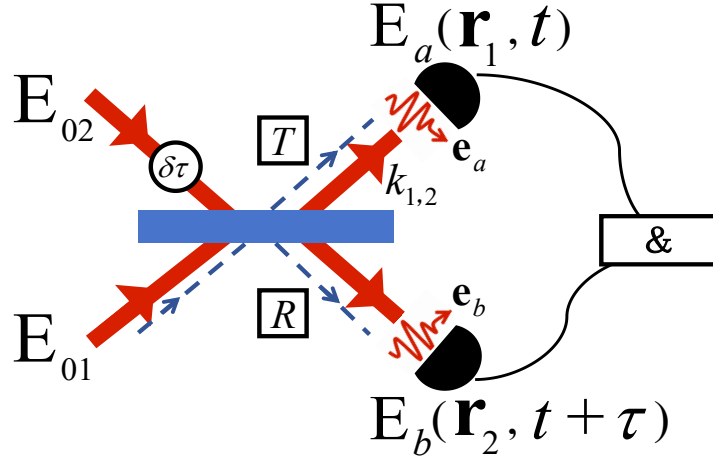


Figure 1: The schematic of the photon detection setup, where two detectors are placed at positions  $\mathbf{r}_1$  and  $\mathbf{r}_2$ , with polarization detection directions  $\mathbf{e}_a$  and  $\mathbf{e}_b$ , respectively.

operator is conventionally decomposed into the positive- and negative-frequency components, such that:

$$\hat{\mathbf{E}}(\mathbf{r}, t) = \hat{\mathbf{E}}^{(+)}(\mathbf{r}, t) + \hat{\mathbf{E}}^{(-)}(\mathbf{r}, t). \quad (2)$$

The components can be expanded by a set of normal modes according to the modal approach

$$\begin{aligned} \hat{\mathbf{E}}^{(+)}(\mathbf{r}, t) &= \sum_n C \sqrt{\omega_n} \mathbf{E}_n(\mathbf{r}) \hat{a}_n(t) \\ &= \sum_n C \sqrt{\omega_n} \mathbf{E}_n(\mathbf{r}) e^{-i\omega_n t} \hat{a}_n \end{aligned} \quad (3)$$

$$\begin{aligned} \hat{\mathbf{E}}^{(-)}(\mathbf{r}, t) &= \sum_n C \sqrt{\omega_n} \mathbf{E}_n^*(\mathbf{r}) \hat{a}_n^\dagger(t) \\ &= \sum_n C \sqrt{\omega_n} \mathbf{E}_n^*(\mathbf{r}) e^{i\omega_n t} \hat{a}_n^\dagger \end{aligned} \quad (4)$$

where  $\omega_n$  and  $C$  are the  $n$ -th eigenfrequency of the modal field expansion and the constant coefficient.  $\mathbf{E}_n$  and  $\hat{a}_n$  are the corresponding normal modes and annihilation operators, respectively.

In order to explore the quantum characteristics of electromagnetic fields, the quantity under investigation is the probability of joint photodetection, which can be mathematically modeled as the correlation function. The photodetection scheme with two detectors located at  $\mathbf{r}_1$  and  $\mathbf{r}_2$  is illustrated in Fig. 1. The first-order correlation function evaluating the probability to detect one photon at the position  $\mathbf{r}_1$  with the polarization  $\mathbf{e}_a$ , is defined as the expectation value of the field operators

$$G_a^{(1)}(\mathbf{r}_1, t) = \langle \Psi | \hat{E}_a^-(\mathbf{r}_1, t) \hat{E}_a^+(\mathbf{r}_1, t) | \Psi \rangle \quad (5)$$

where  $\hat{E}_a^-(\mathbf{r}_1, t) = \hat{\mathbf{E}}^-(\mathbf{r}_1, t) \cdot \mathbf{e}_a = \hat{E}_a^+(\mathbf{r}_1, t)^\dagger$  is the projection of the negative-frequency part of the field operator on the polarization vector. The second-order correlation function corresponding to the fourth-order field interference yields the joint probability to detect one photon at the position  $\mathbf{r}_1$  with the polarization  $\mathbf{e}_a$  and the other photon at the position  $\mathbf{r}_2$  with the polarization  $\mathbf{e}_b$

$$G_{ab}^{(2)}(\mathbf{r}_1, \mathbf{r}_2, t) = \langle \Psi | \hat{E}_a^-(\mathbf{r}_1, t) \hat{E}_b^-(\mathbf{r}_2, t) \hat{E}_b^+(\mathbf{r}_2, t) \hat{E}_a^+(\mathbf{r}_1, t) | \Psi \rangle. \quad (6)$$

To assess the degree of quantum coherence, the second-order normalized correlation function [51, 52] could be introduced

$$\begin{aligned} g_{ab}^{(2)}(\mathbf{r}_1, \mathbf{r}_2, t) &= \frac{G_{ab}^{(2)}(\mathbf{r}_1, \mathbf{r}_2, t)}{G_a^{(1)}(\mathbf{r}_1, t) G_b^{(1)}(\mathbf{r}_2, t)} \\ &= \frac{\langle \Psi | \hat{E}_a^-(\mathbf{r}_1, t) \hat{E}_b^-(\mathbf{r}_2, t) \hat{E}_b^+(\mathbf{r}_2, t) \hat{E}_a^+(\mathbf{r}_1, t) | \Psi \rangle}{\langle \Psi | \hat{E}_a^-(\mathbf{r}_1, t) \hat{E}_a^+(\mathbf{r}_1, t) | \Psi \rangle \langle \Psi | \hat{E}_b^-(\mathbf{r}_2, t) \hat{E}_b^+(\mathbf{r}_2, t) | \Psi \rangle} \end{aligned} \quad (7)$$

## 2.1 The correlation function in the frequency domain

In the analysis of far-field quantum effects, the angular distribution and interference effects can be fully characterized by the field response at a single frequency, with contributions from other frequencies being comparatively negligible (Given that experimental single-photon sources are typically ultra-narrowband). Considering a two-photon quantum state, the photons occupy two distinct scattering eigenmodes. The total quantum state is represented by  $|\Psi\rangle_{12} = \sum_{nn'} \phi_{nk_1} \phi_{n'k_2} \hat{a}_n^\dagger \hat{a}_{n'}^\dagger |0\rangle \otimes |0\rangle$ , which does not evolve in time. The weight functions  $\phi_{nk_{1,2}}$  are normalized, sufficiently distinguishable, and sharply peaked around  $k_{1,2}$ , ensuring that their contribution to any well-behaved function is dominated by  $k_{1,2}$  ( $\sum_n \phi_{nk_{1,2}} E_n \propto E_{k_{1,2}}$ ) [31]. Accordingly, the multimode expansion of the field operators, upon acting on the quantum state, can be approximated by retaining only the dominant contributions from the two scattering modes with the wave numbers of  $k_1$  and  $k_2$ , such that

$$\hat{E}_a^-(\mathbf{r}_1, t) = C\sqrt{\omega_{k_1}} E_{ak_1}^*(\mathbf{r}_1) e^{i\omega_{k_1} t} \hat{a}_{k_1}^\dagger + C\sqrt{\omega_{k_2}} E_{ak_2}^*(\mathbf{r}_1) e^{i\omega_{k_2} t} \hat{a}_{k_2}^\dagger \quad (8)$$

$$\hat{E}_b^-(\mathbf{r}_2, t) = C\sqrt{\omega_{k_1}} E_{bk_1}^*(\mathbf{r}_2) e^{i\omega_{k_1} t} \hat{a}_{k_1}^\dagger + C\sqrt{\omega_{k_2}} E_{bk_2}^*(\mathbf{r}_2) e^{i\omega_{k_2} t} \hat{a}_{k_2}^\dagger. \quad (9)$$

The formula for the positive-frequency components can likewise be obtained. Based on the standard bosonic relations:  $\hat{a}_k|p\rangle_k = \sqrt{p}|p-1\rangle_k$  with  $\hat{a}_k|0\rangle_k = 0$ ,  $\hat{a}_k^\dagger|p\rangle_k = \sqrt{p+1}|p+1\rangle_k$ ,  $p$  denotes the non-negative photon number, the expression for  $g_{ab}^{(2)}$  can be further derived into the form:

$$\begin{aligned} g_{ab}^{(2)}(\mathbf{r}_1, \mathbf{r}_2) &= U_1 + U_2 + U_3 + U_4 \\ &= \frac{\omega_{k_1} \omega_{k_2} |E_{ak_1}(\mathbf{r}_1) E_{bk_2}(\mathbf{r}_2) + E_{ak_2}(\mathbf{r}_1) E_{bk_1}(\mathbf{r}_2)|^2}{\sum_{n=1,2} \omega_{k_n} |E_{ak_n}(\mathbf{r}_1)|^2 \sum_{n=1,2} \omega_{k_n} |E_{bk_n}(\mathbf{r}_2)|^2} \end{aligned} \quad (10)$$

where

$$U_1 = \frac{\omega_{k_1} \omega_{k_2} [E_{ak_1}^*(\mathbf{r}_1) E_{bk_2}^*(\mathbf{r}_2) E_{ak_1}(\mathbf{r}_1) E_{bk_2}(\mathbf{r}_2)]}{\sum_{n=1,2} \omega_{k_n} |E_{ak_n}(\mathbf{r}_1)|^2 \sum_{n=1,2} \omega_{k_n} |E_{bk_n}(\mathbf{r}_2)|^2} \quad (11)$$

$$U_2 = \frac{\omega_{k_1} \omega_{k_2} [E_{ak_1}^*(\mathbf{r}_1) E_{bk_2}^*(\mathbf{r}_2) E_{ak_2}(\mathbf{r}_1) E_{bk_1}(\mathbf{r}_2)]}{\sum_{n=1,2} \omega_{k_n} |E_{ak_n}(\mathbf{r}_1)|^2 \sum_{n=1,2} \omega_{k_n} |E_{bk_n}(\mathbf{r}_2)|^2} \quad (12)$$

$$U_3 = \frac{\omega_{k_1} \omega_{k_2} [E_{ak_2}^*(\mathbf{r}_1) E_{bk_1}^*(\mathbf{r}_2) E_{ak_1}(\mathbf{r}_1) E_{bk_2}(\mathbf{r}_2)]}{\sum_{n=1,2} \omega_{k_n} |E_{ak_n}(\mathbf{r}_1)|^2 \sum_{n=1,2} \omega_{k_n} |E_{bk_n}(\mathbf{r}_2)|^2} \quad (13)$$

$$U_4 = \frac{\omega_{k_1} \omega_{k_2} [E_{ak_2}^*(\mathbf{r}_1) E_{bk_1}^*(\mathbf{r}_2) E_{ak_2}(\mathbf{r}_1) E_{bk_1}(\mathbf{r}_2)]}{\sum_{n=1,2} \omega_{k_n} |E_{ak_n}(\mathbf{r}_1)|^2 \sum_{n=1,2} \omega_{k_n} |E_{bk_n}(\mathbf{r}_2)|^2}. \quad (14)$$

It is evident that the operator constrains the expression to four surviving terms of the field product;  $U_2$  and  $U_3$  are the intensity interference terms arising from the distinguishability of the two sources. Its value remains bounded between 0 and 1, regardless of the photonic environment, reflecting the antibunching characteristic intrinsic to quantum emitters[53, 54]. In contrast, incoherent classical emitters exhibited autocorrelation values exceeding unity under the conditions  $\mathbf{r}_1 = \mathbf{r}_2$  and  $\mathbf{e}_a = \mathbf{e}_b$ [55].

## 2.2 The normalized coincidence number function in the time domain

Furthermore, for the purpose of investigating the experimentally observed coincidence measurements at the time domain, the derivation of the expected number  $N_c$  about the function of the externally controlled optical path-delay  $\delta\tau$  is carried out by referring to the method presented in [27]. Firstly, considering the standard operation of the phase-asymmetric beam splitter shown in Fig. 1, the fields at the detection positions are expressed as linear combinations of the incident fields via the reflection ( $R$ ) and transmission ( $T$ ) coefficients of the beam splitter as follows:

$$\hat{E}_a^{(+)}(\mathbf{r}_1, t) = \sqrt{T} \hat{E}_{01}^{(+)}(t) + i\sqrt{R} \hat{E}_{02}^{(+)}(t + \delta\tau) \quad (15)$$

$$\hat{E}_b^{(+)}(\mathbf{r}_2, t + \tau) = \sqrt{T} \hat{E}_{02}^{(+)}(t + \tau) + i\sqrt{R} \hat{E}_{01}^{(+)}(t + \tau - \delta\tau) \quad (16)$$

where  $t$  and  $t + \tau$  denote the respective photon detection times at the two detectors. Secondly, in order to evaluate the second-order correlation function (6), substituting the state function and the field operators in (1)-(4), the correlation function is equivalently transformed into an integration over the continuous frequency spectrum of the excitation photon sources  $\hat{E}_{01}^{(+)}$  and  $\hat{E}_{02}^{(+)}$ . In this representation, the temporal delay  $\tau$  enters through exponential phase factors  $e^{\pm i\omega\tau}$ ,

so that  $G_{ab}^{(2)}$  can be reformulated as a combination of the functions  $h(\tau)$  and  $h(2\delta\tau - \tau)$  as shown in the following equation:

$$G_{ab}^{(2)}(\mathbf{r}_1, \mathbf{r}_2, \tau) = K \{ T^2 |h(\tau)|^2 + R^2 |h(2\delta\tau - \tau)|^2 - RT [h^*(\tau)h(2\delta\tau - \tau)] - RT [h(\tau)h^*(2\delta\tau - \tau)] \} \quad (17)$$

where  $h(\tau)$  has the form  $e^{-\frac{\tau^2}{2\sigma^2}} \cdot e^{-i\omega_0\tau}$  characterized by a bandwidth of  $1/\sigma$ , given that the excitation photon sources in experiment employ ultra-narrowband Gaussian pulses at the central frequency  $\omega_0$ , and  $K$  is an integration constant. Finally, coincidence measurements are typically performed over temporal windows much longer than the characteristic correlation time, thus allowing the probability to be integrated over the entire  $\tau$  domain, which yields  $N_c(\delta\tau) = \int_{-\infty}^{\infty} G_{ab}^{(2)}(\mathbf{r}_1, \mathbf{r}_2, \tau) d(\tau)$ .

In order to elucidate the interplay between angle-dependent field distributions and  $N_c$ , a theoretical framework is formulated to evaluate the joint detection probability in distinct far-field regimes. The response coefficients, initially characterized by  $R$  and  $T$ , across different frequency components are approximated by the far-field amplitudes  $E_{ak1,2}(\mathbf{r}_1)$  and  $E_{bk1,2}(\mathbf{r}_2)$  evaluated at  $\omega_{k1} = \omega_{k2} = \omega_0$ , while the ultra-narrowband spectral profile of the photon wave packets is fully preserved. The far-field amplitudes are obtained via the spatial Green's function formalism, inherently containing all the information about the surrounding environment. Under this theoretical framework,  $N_c$  is normalized by a factor  $D_c$  to define  $\tilde{N}_c$ , such that its value tends to unity as the time delay approaches infinity:

$$\tilde{N}_c(\delta\tau) = \frac{N_1(\delta\tau) + N_2(\delta\tau) + N_3(\delta\tau) + N_4(\delta\tau)}{D_c(\delta\tau)} \quad (18)$$

where

$$N_1(\delta\tau) = \int_{-\infty}^{\infty} \{ |E_{ak1}(\mathbf{r}_1)E_{bk2}(\mathbf{r}_2)|^2 |h(\tau)|^2 \} d(\tau) \quad (19)$$

$$N_2(\delta\tau) = \int_{-\infty}^{\infty} \{ |E_{bk1}(\mathbf{r}_2)E_{ak2}(\mathbf{r}_1)|^2 |h(2\delta\tau - \tau)|^2 \} d(\tau) \quad (20)$$

$$N_3(\delta\tau) = \int_{-\infty}^{\infty} \{ E_{ak1}(\mathbf{r}_1)E_{bk2}(\mathbf{r}_2)E_{bk1}^*(\mathbf{r}_2)E_{ak2}^*(\mathbf{r}_1) [h(\tau)h^*(2\delta\tau - \tau)] \} d(\tau) \quad (21)$$

$$N_4(\delta\tau) = \int_{-\infty}^{\infty} \{ E_{ak1}^*(\mathbf{r}_1)E_{bk2}^*(\mathbf{r}_2)E_{bk1}(\mathbf{r}_2)E_{ak2}(\mathbf{r}_1) [h^*(\tau)h(2\delta\tau - \tau)] \} d(\tau) \quad (22)$$

$$D_c(\delta\tau) = \int_{-\infty}^{\infty} \{ [|E_{ak1}(\mathbf{r}_1)|^2 |h(\tau)| + |E_{ak2}(\mathbf{r}_1)|^2 |h(2\delta\tau - \tau)|] \cdot [|E_{bk2}(\mathbf{r}_2)|^2 |h(\tau)| + |E_{bk1}(\mathbf{r}_2)|^2 |h(2\delta\tau - \tau)|] \} d(\tau). \quad (23)$$

The temporal envelope of the Gaussian excitation pulses defines the coherence time of the generated photons, which in turn determines the characteristic width of the interference curve. Notably, this study emphasizes the comparative behavior of the normalized curves, treating the temporal axis as a scalable parameter that depends on the specific implementation details of the experimental system.

### 2.3 Numerical method

In order to extract the far-field results at the detection positions for a specific frequency, the VIE method is employed for numerical simulations in this work. The response is governed by the relation  $\mathbf{E}^{tot} - \mathbf{E}^{sca} = \mathbf{E}^{inc}$ , the total and scattered fields are both expressed in terms of the induced volumetric polarization current  $\mathbf{J}^s$  as follows:

$$-\frac{\mathbf{J}^s(\mathbf{r})}{i\omega(\varepsilon - \varepsilon_0)} - i\omega\mu_0 \int_V \overleftrightarrow{\mathbf{G}}(\mathbf{r}, \mathbf{r}') \cdot \mathbf{J}^s(\mathbf{r}') dv' = \mathbf{E}^{inc} \quad (24)$$

where  $\overleftrightarrow{\mathbf{G}}(\mathbf{r}, \mathbf{r}') = \left( \overleftrightarrow{\mathbf{I}} + \frac{1}{k_0^2} \nabla \nabla \right) \frac{e^{ik_0|\mathbf{r}-\mathbf{r}'|}}{4\pi|\mathbf{r}-\mathbf{r}'|}$  is the dyadic Green's function of free space;  $\varepsilon_0$ ,  $\mu_0$  represent the permittivity and permeability of free space, and  $\varepsilon$  denotes the permittivity of the dielectric material. Once the polarization current is determined, the far field can be evaluated based on the asymptotic form of the dyadic Green's function in the radiation zone:

$$\mathbf{E}_{\infty}^{sca}(\hat{\mathbf{r}}) \propto \int_V [\hat{\mathbf{r}} \times (\mathbf{J}^s(\mathbf{r}') \times \hat{\mathbf{r}})] e^{-ik_0\hat{\mathbf{r}} \cdot \mathbf{r}'} d\mathbf{r}' \quad (25)$$

where  $\hat{\mathbf{r}}$  denotes the unit vector in the observation direction. The matrix equation (24) derived for the  $\mathbf{J}^s$  can be efficiently solved using the bi-conjugate gradient stabilized iterative scheme[56], particularly when paired with FFT-accelerated matrix-vector operations for large-scale systems. For the dielectric metasurfaces, applying block preconditioners in conjunction with parallel computing enables further improvements in computational efficiency[49].

### 3 Results

In this section, we investigate two distinct scenarios exhibiting observable quantum effects: photon-pair scattering from a dielectric sphere, and the generation of spatial-polarization entanglement via a space-variant Pancharatnam–Berry phase metasurface. They reveal the angular distribution of the HOM interference, where the structure serves as a three-dimensional beam splitter.

#### 3.1 Dielectric Sphere

In order to study the joint detection probability, we consider the interference effects of a two-photon state on a dielectric sphere. Each photon is assumed to occupy normalized, orthogonal eigenmodes of the outgoing scattering E-field. The incident single photon pairs: one  $y$ -polarized wave traveling along the  $x$ -direction ( $k_1 = k\mathbf{e}_x$ ), and the other  $x$ -polarized wave propagating along the  $y$ -direction ( $k_2 = k\mathbf{e}_y$ ). Hence, (10) is reformulated as:

$$g_{zz}^{(2)}(\mathbf{r}_1, \mathbf{r}_2) = \frac{\omega_{k_1} \omega_{k_2} |E_{zk_1}(\mathbf{r}_1) E_{zk_2}(\mathbf{r}_2) + E_{zk_2}(\mathbf{r}_1) E_{zk_1}(\mathbf{r}_2)|^2}{\sum_{n=1,2} \omega_{k_n} |E_{zk_n}(\mathbf{r}_1)|^2 \sum_{n=1,2} \omega_{k_n} |E_{zk_n}(\mathbf{r}_2)|^2}. \quad (26)$$

Since the incident plane-wave component generally outweighs the scattered contribution in the far field, only  $z$ -polarized photons are detected ( $a = b = z$ ) to extract the correlation from the scattered part alone[31]. Given that the detectors are positioned in the far-field region of the sphere, (26) characterizes the dependence of the normalized second-order correlation function on the polar and azimuthal angles  $(\theta, \phi)$ .

The validation of the numerical method is performed by comparing the results with the analytical solution for an electrically small dielectric sphere, as presented in [31]. Based on the VIE method, the sphere is modeled with the relative permittivity  $\epsilon = 2.1$  at 750 THz. The two polar positions are fixed at  $\theta_1 = 45^\circ$ ,  $\theta_2 = 135^\circ$ . The schematic illustrating the two-photon state and the positions of detectors is shown in Fig. 2(a). The  $z$  component of the far-field electric field could be calculated by the polarization current based on (25) and then  $g_{zz}^{(2)}$  is evaluated based on (26). The red dashed lines in Fig. 2 show the numerical results of  $g_{zz}^{(2)}(\phi_1, \phi_2)$  for  $\phi_2 = 135^\circ$ , plotted as a function of the azimuthal angle  $\phi_1$  of the first detector, with  $\phi_1 \in [0^\circ, 90^\circ]$ . The detection region matches the angular range marked by the red line in Fig. 2(b). For spheres with radii of 60 nm, 110 nm, and 123 nm, the comparison between the numerical simulation (red) and the reference result (blue) shows excellent agreement, as quantified by the relative L2-norm errors of 2.81%, 2.73% and 1.59%, thereby confirming the accuracy and reliability of the algorithm. It is evident that spheres with different radii induce significant variations in the angular dependence of  $g_{zz}^{(2)}$ . Additionally, the normalized second-order correlation function for the sphere at  $r = 60$  nm is depicted in the inset of Fig. 2(b) as an angular map over the azimuthal angles  $\phi_1$  and  $\phi_2$  of the detectors. The blue diagonal stripes correspond to the HOM destructive interference. At the two detector positions indicated by the purple markers, the scattered field amplitudes arising from one of the sources are identically zero. This behavior is distinct from the HOM-like interference patterns observed at other positions. In analogy to the quantum second-order correlation function, the classical intensity correlation function is defined to describe the coherence properties of deterministic electromagnetic fields. Its mathematical form is given by:

$$P_{zz}^{(2)}(\mathbf{r}_1, \mathbf{r}_2) = \frac{E_z^*(\mathbf{r}_1) E_z^*(\mathbf{r}_2) E_z(\mathbf{r}_2) E_z(\mathbf{r}_1)}{\omega_{k_1} \omega_{k_2} |E_{zk_1}(\mathbf{r}_1) + E_{zk_2}(\mathbf{r}_1)|^2 |E_{zk_1}(\mathbf{r}_2) + E_{zk_2}(\mathbf{r}_2)|^2} \quad (27)$$

It is normalized by dividing by the maximum intensity value. The comparison of the normalized fourth-order correlation of fields for the classical and quantum scattering is shown in Fig. 3. The classical result reveals distinct interference features with periodic peaks and valleys, indicative of constructive and destructive interference between the two fields. These interference patterns exhibit symmetry and are characterized by localized regions of field enhancement and suppression, typical of classical wave phenomena. In contrast, the quantum correlation function exhibits smoother, oscillatory behavior, reflecting the intrinsic coherence and non-local properties of quantum light. The phase-dependent oscillations are at the origin of the HOM dip.

Moreover, the normalized coincidence counts  $\tilde{N}_c$  as a function of the initial photon time delay is investigated. According to the angular map of Fig. 2(b), four representative angular positions were selected, at which the values of  $g_{zz}^{(2)}(\phi_1, \phi_2)$  exhibit substantial differences. Substituting the electric-field coefficients at the specified angular positions into (18) yields the respective coincidence counts  $\tilde{N}_c$  as functions of the time delay  $\delta\tau$ , which are shown in Fig. 4(b). It is evident that the dip depth in the coincidence profile is directly governed by the value of  $g_{zz}^{(2)}(\phi_1, \phi_2)$ . The red curve exhibits the vanishing of two-photon coincidence rate at zero delay time which is widely referred to as the HOM dip. In this case, the two photon wave packets are temporally indistinguishable, allowing for the perfect fourth-order interference. The  $g_{zz}^{(2)}$  values corresponding to the gray curve remain between 0 and 1, resulting in a shallower dip depth compared to the red curve. Similarly, the blue curve corresponds to the position where  $g_{zz}^{(2)} = 1$ , indicating the absence of quantum

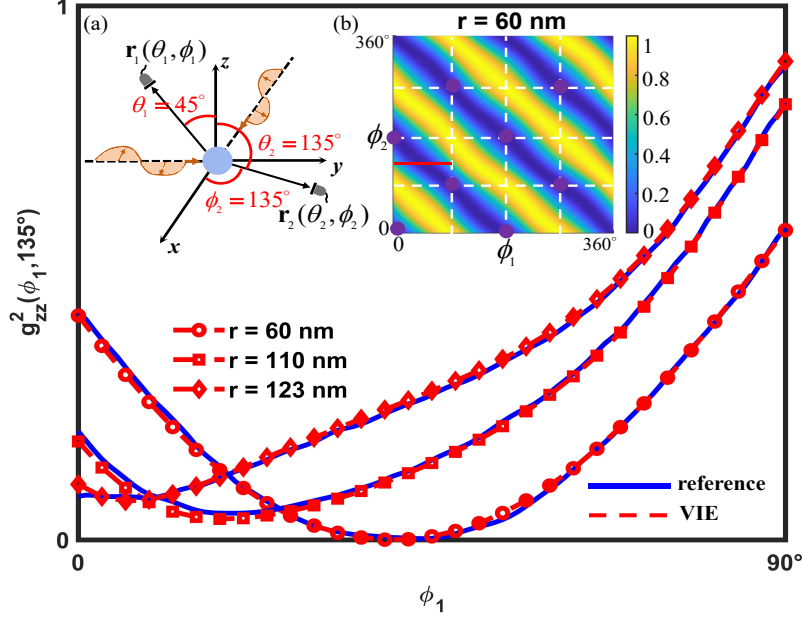


Figure 2: Normalized second-order correlation function  $g_{zz}^{(2)}(\phi_1, \phi_2 = 135^\circ)$  for spheres with different radii  $r = 60$  nm, 110 nm, 123 nm. (a) The schematic illustrating the two-photon state and the positions of detectors with respect to the dielectric sphere. (b) Normalized second-order correlation function  $g_{zz}^{(2)}(\phi_1, \phi_2)$  for the sphere at  $r = 60$  nm as a function of the azimuthal positions of the two detectors fixed at  $\theta_1 = 45^\circ$ ,  $\theta_2 = 135^\circ$ .

interference. As a result, the coincidence probability  $\tilde{N}_c$  remains at unity regardless of the time delay, since the two photons are fully distinguishable and the expectation value asymptotically approaches the classical limit. Under the normalization assumption, as the time delay increases beyond a certain threshold, all the curves approach the value of unity. Interestingly, although the purple curve also corresponds to  $g_{zz}^{(2)} = 0$ , this vanishing arises not from interference effects but from the intrinsic symmetry of the sphere, only certain multipolar modes can be excited by a given incident polarization. As a result, for the specific far-field observation angles, the induced dipolar moments do not radiate any  $z$ -polarized components for one of the incident polarizations. In this case, the joint detection involves effectively only a single photon. Since second-order correlation measurements inherently require simultaneous contributions from both photons, the resulting measurement no longer constitutes a genuine two-photon process. Consequently, the coincidence counts vanish across all time delays, not as a result of destructive interference, but due to the lack of two-photon participation in the detection event. As illustrated in Figs. 4(a) and (b), both the angular dependence in the frequency domain and the coincidence counts in the time domain exhibit the HOM effect. The resulting  $\tilde{N}_c$  curve directly correlates with  $g_{zz}^{(2)}$  at different detection positions. Notably, when  $g_{zz}^{(2)} = 0$ , the origin of the vanishing—whether stemming from interference effects or intrinsic field properties—can be distinguished by the shape of the  $\tilde{N}_c$  curve.

### 3.2 Dielectric Metasurface

Metasurfaces have revolutionized optical wavefront engineering by enabling unprecedented control over the amplitude, phase, polarization, and spectral content of light. Their intrinsic ability to manipulate light at the nanoscale has given rise to a wide range of applications, including flat optics[57][58], holography[59], beam shaping, polarization control, and dispersion engineering. In recent years, the same structural advantages have sparked growing interest in deploying metasurfaces for quantum state manipulation.

In this work, a polarization-converting metasurface based on the space-variant Pancharatnam–Berry-phase (PBP) profile is designed to deflect the incident plane-wave into the output directions under angles of  $\pm 10^\circ$ . Given horizontally ( $|H\rangle$ ) and vertically ( $|V\rangle$ ) polarized input, the output states are left ( $|L\rangle$ ) and right ( $|R\rangle$ ) circularly polarized. The

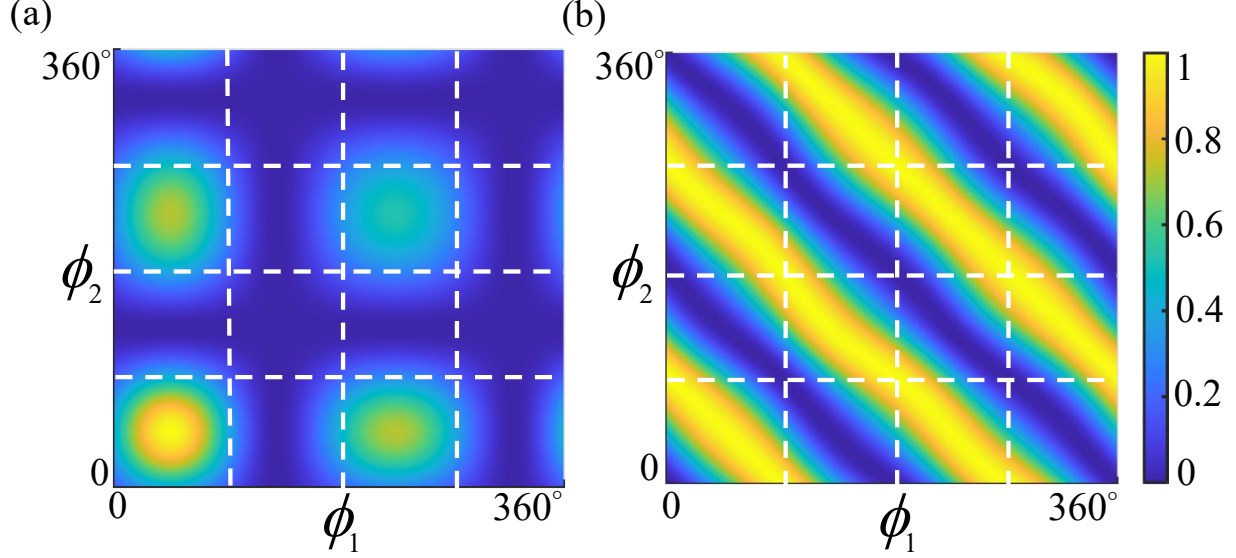


Figure 3: The angular map of the normalized fourth-order correlation of fields. (a) classical scattering. (b) quantum scattering.

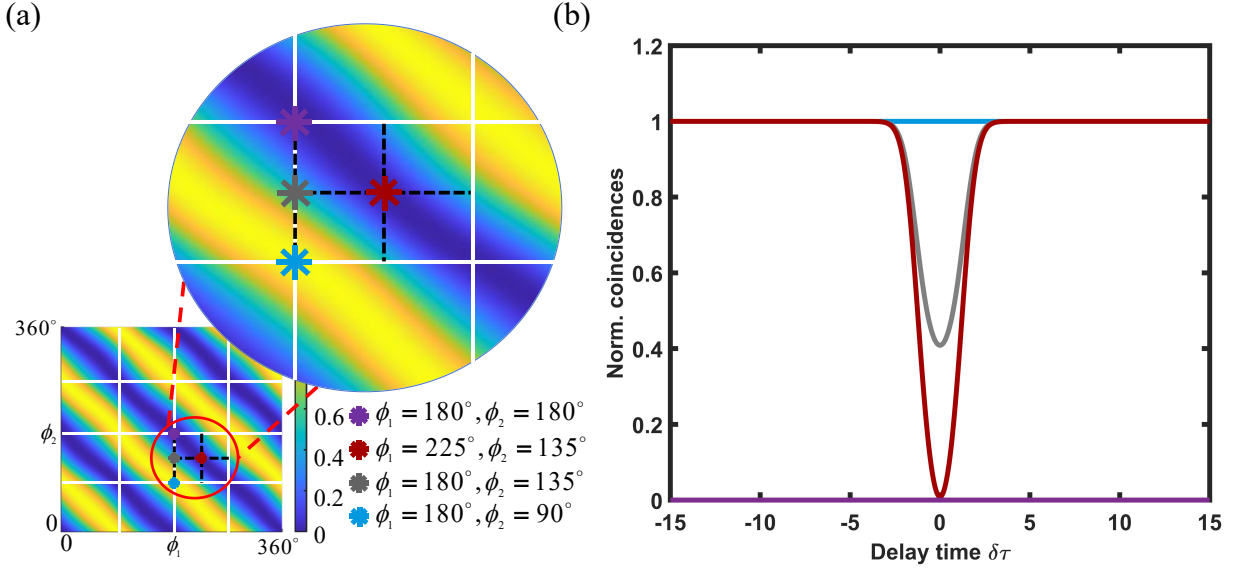


Figure 4: (a) Four representative detection positions in the angular map:  $\phi_1 = 180^\circ, \phi_2 = 180^\circ$ ;  $\phi_1 = 225^\circ, \phi_2 = 135^\circ$ ;  $\phi_1 = 180^\circ, \phi_2 = 135^\circ$ ;  $\phi_1 = 180^\circ, \phi_2 = 90^\circ$ . (b) Normalized coincidence counts  $\tilde{N}_c$  between the two detection positions for a variation of the initial photon time delay  $\delta\tau$ .

positive-frequency components of the electric-field operators can be written, according to the classical relation:

$$\begin{aligned}\hat{E}_L^\dagger &= \frac{1}{\sqrt{2}} \left( \hat{E}_H^\dagger + i \cdot \hat{E}_V^\dagger \right) \\ \hat{E}_R^\dagger &= \frac{1}{\sqrt{2}} \left( \hat{E}_H^\dagger - i \cdot \hat{E}_V^\dagger \right).\end{aligned}\tag{28}$$

The initial quantum state in the circular basis can be derived to be:

$$|\Psi\rangle = \hat{E}_H^\dagger \hat{E}_V^\dagger |0\rangle \otimes |0\rangle = -\frac{i}{2} \left( \hat{E}_L^\dagger \hat{E}_L^\dagger - \hat{E}_R^\dagger \hat{E}_R^\dagger \right) |0\rangle \otimes |0\rangle\tag{29}$$



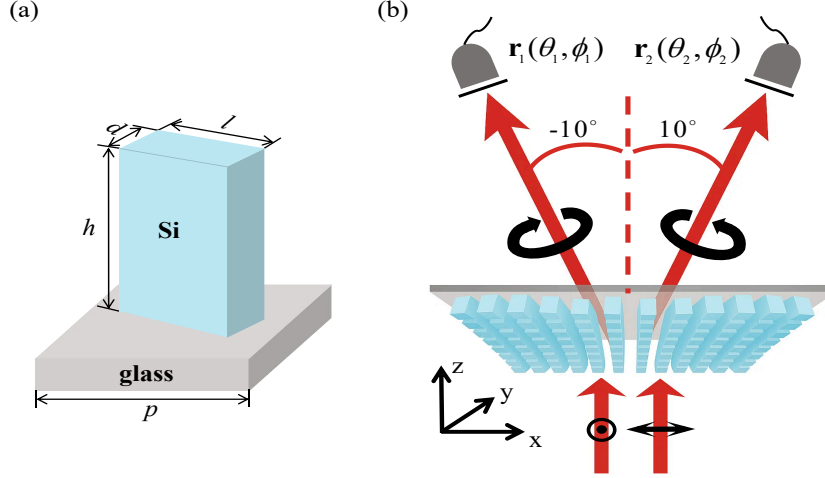


Figure 5: (a) The geometric schematic of the metasurface unit cell. (b) The schematic of the two-photon state and the positions of detectors with respect to the PBP metasurface.

which corresponds to a two-photon NOON state. The metasurface inducing a spatial separation of orthogonal polarization components gives rise to a path-entangled quantum state. For the evaluation of the normalized second-order correlation function, the two photons occupy orthogonally polarized scattering eigenmodes aligned with the  $x$ - and  $y$ -axis directions (i.e.,  $H$  and  $V$  polarizations), in analogy with the dielectric sphere case. For the metasurface case, the projections of the far-field onto the polarization vectors are computed by

$$\begin{aligned} E_L &= \frac{1}{\sqrt{2}} (E_\theta + iE_\phi) \\ E_R &= \frac{1}{\sqrt{2}} (E_\theta - iE_\phi). \end{aligned} \quad (30)$$

Substituting the left and right circularly polarized components of the far-field electric field into (10), the normalized second-order correlation function  $g_{LR}^{(2)}(\mathbf{r}_1, \mathbf{r}_2)$  at different detection angles could be obtained by the equation

$$g_{LR}^{(2)}(\mathbf{r}_1, \mathbf{r}_2) = \frac{\omega_{k_H} \omega_{k_V} |E_{Rk_H}(\mathbf{r}_1) E_{Lk_V}(\mathbf{r}_2) + E_{Rk_V}(\mathbf{r}_1) E_{Lk_H}(\mathbf{r}_2)|^2}{\sum_{n=H,V} \omega_{k_n} |E_{Rk_n}(\mathbf{r}_1)|^2 \sum_{n=H,V} \omega_{k_n} |E_{Lk_n}(\mathbf{r}_2)|^2}. \quad (31)$$

Referring to the structural parameters presented in [12], the nanofins of the PBP metasurface in Fig. 5(a) are designed as: the periodicity  $p = 667$  nm, the nanofin height  $h = 830$  nm, length  $l = 486$  nm, and the width  $d = 219$  nm. For the simulation, we assumed a refractive index of  $n_{Si} = 3.44$  for the silicon nanofins and of  $n_{glass} = 2.25$  for the substrate at a wavelength of 1550 nm. The local rotation angle of each nanofin is determined by the PBP design rule, i.e.,

$$\theta_m = \frac{1}{2} k_0 \sin(\theta_t) \cdot m \cdot p \quad (32)$$

where  $\theta_t$  is the desired deflection angle  $10^\circ$ ,  $k_0$  is the vacuum wavenumber, and  $\theta_m$  denotes the local rotation angle of the  $m$ -th nanofin unit cell. Therefore, a rotational increment of  $13.44^\circ$  between adjacent nanofin unit cells can be obtained. The structure consists of groups of 13 nanofin unit cells aligned laterally, periodically arranged into 7 groups along both the  $x$ - and  $y$ -directions. It acts as a circular polarization beam separator, deflecting right-handed circularly polarized waves toward  $-10^\circ$  and left-handed ones toward  $10^\circ$ . The schematic of the metasurface detection setup is shown in Fig. 5(b).

The VIE method is used to simulate the structure with electrical dimensions of  $40\lambda_0 \times 12\lambda_0 \times 2\lambda_0$  ( $\lambda_0$  is the wavelength of free space) and a spatial discretization of 62 grids per  $\lambda_0$ . Thus the total number of mesh elements is 18,013,710 and that of unknown currents along the three dimensions is 54,041,130. The resulting dense matrix requires intensive computational time to solve. Considering the inherent structural regularity and periodicity, the structure is uniformly partitioned into  $7 \times 7$  blocks for the implementation of the parallel block preconditioner. The solution of the preconditioned block matrices and the FFT-based operations are executed in a parallel manner, utilizing all 24 available threads to fully exploit the multicore architecture[49]. The preconditioner significantly improved the computational efficiency, reducing the solution time from 31.9 hours (without preconditioner) to 24 hours (with preconditioner). By

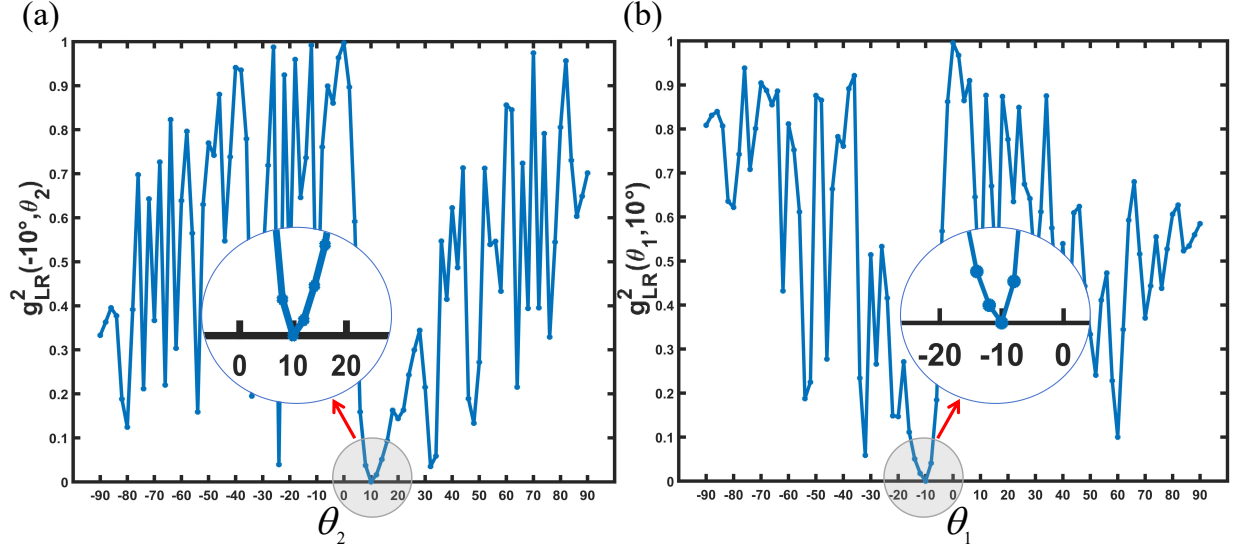


Figure 6: (a) Normalized second-order correlation function  $g_{LR}^{(2)}(\theta_1 = -10^\circ, \theta_2)$  as a function of  $\theta_2$ . (b) Normalized second-order correlation function  $g_{LR}^{(2)}(\theta_1, \theta_2 = 10^\circ)$  as a function of  $\theta_1$ .

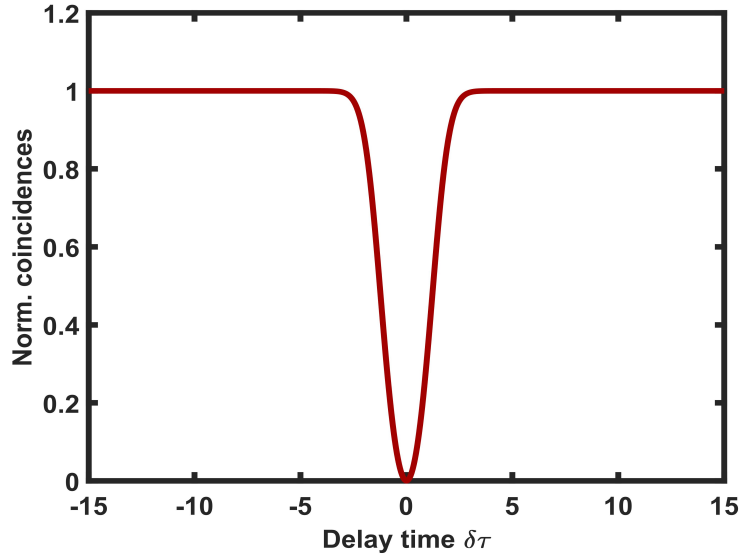


Figure 7: Normalized coincidence counts  $\tilde{N}_c$  between the two detection positions for a variation of the initial photon time delay  $\delta\tau$ .

fixing the azimuthal angles of detectors  $\phi_1 = 180^\circ$ ,  $\phi_2 = 0^\circ$ , the Figs. 6(a) and (b) respectively show the numerical results of  $g_{LR}^{(2)}(\theta_1, \theta_2)$  as a function of  $\theta_2$  with  $\theta_1$  fixed at  $-10^\circ$ , and as a function of  $\theta_1$  with  $\theta_2$  fixed at  $10^\circ$ . It can be observed that a vanishing correlation function  $g_{LR}^{(2)}(\mathbf{r}_1, \mathbf{r}_2) = 0$  arises at the specific angular configuration  $\theta_1 = -10^\circ$ ,  $\theta_2 = 10^\circ$ , indicating completely destructive two-photon interference, i.e., the HOM interference effect. The characteristics of  $g_{LR}^{(2)}$  exhibit pronounced sensitivity to the angular variations, which could serve as a reliable approach to investigate the scattering response of the structure.

Also, we calculate the normalized coincidence counts  $\tilde{N}_c$  as a function of the initial photon time delay  $\delta\tau$  using (18). Substituting the electric-field coefficients at the vanishing point, the results are depicted in Fig. 7. Clearly, the curve also exhibits a characteristic HOM dip. The shape of the resulting curve is consistent with the experimental measurements presented in [12]. The bandwidth of the wave is directly determined by the temporal width parameter of the photon

Gaussian pulse. It indicates that when no time delay  $\delta\tau$  is present between identically distributed inputs, perfect quantum behavior arises, i.e., path-entangled photon pairs are generated. As the time delay increases and the photons become increasingly distinguishable, the expectation value gradually converges to the classical limit where each photon exits through either output with equal probability.

## 4 Conclusion

This paper investigates the far-field interference associated with the HOM effect. By calculating the classical electric fields using the VIE method and substituting them into the second-order normalized correlation function  $g^{(2)}$ , the photon interference at different detection (scattered) angles is analyzed. Key findings indicate that the far-field correlation functions exhibit substantial variation with the detection angle, and the angular spectrum distribution differs markedly from classical intensity correlation. Additionally, the value of  $g^{(2)}$  is closely correlated with the shape of the  $\tilde{N}_c$  curve, revealing the direct relationship between angular interference patterns and HOM dip characteristics. Notably,  $g^{(2)}$  is highly sensitive to both the structural dimensions and angles, as observed for different sphere radii and angular scans of metasurfaces. The observed sensitivity provides a diagnostic tool for retrieving material and structural information and capturing subtle perturbations in the underlying design parameters. Our future work will focus on exploring the application of correlation functions in the quantum inverse problems of photonic structures, as well as the coincidence measurement across various angular far-field directions.

## References

- [1] Alexandre Blais, Steven M Girvin, and William D Oliver. Quantum information processing and quantum optics with circuit quantum electrodynamics. *Nature Physics*, 16(3):247–256, 2020.
- [2] Michael A Nielsen and Isaac L Chuang. *Quantum computation and quantum information*. Cambridge university press, 2010.
- [3] Pieter Kok, William J Munro, Kae Nemoto, Timothy C Ralph, Jonathan P Dowling, and Gerard J Milburn. Linear optical quantum computing with photonic qubits. *Reviews of modern physics*, 79(1):135–174, 2007.
- [4] Marlan O Scully and M Suhail Zubairy. *Quantum optics*. Cambridge university press, 1997.
- [5] Ho Trung Dung, Ludwig Knöll, and Dirk-Gunnar Welsch. Spontaneous decay in the presence of dispersing and absorbing bodies: General theory and application to a spherical cavity. *Physical Review A*, 62(5):053804, 2000.
- [6] Stefan Scheel, L Knöll, and D-G Welsch. Spontaneous decay of an excited atom in an absorbing dielectric. *Physical Review A*, 60(5):4094, 1999.
- [7] Peng-fei Qiao, Wei El Sha, Wallace CH Choy, and Weng Cho Chew. Systematic study of spontaneous emission in a two-dimensional arbitrary inhomogeneous environment. *Physical Review A—Atomic, Molecular, and Optical Physics*, 83(4):043824, 2011.
- [8] Michael E Crenshaw. Comparison of quantum and classical local-field effects on two-level atoms in a dielectric. *Physical Review A—Atomic, Molecular, and Optical Physics*, 78(5):053827, 2008.
- [9] Thomas Gerard Philbin. Casimir effect from macroscopic quantum electrodynamics. *New Journal of Physics*, 13(6):063026, 2011.
- [10] Rudolf Bratschitsch and Alfred Leitenstorfer. Artificial atoms for quantum optics. *Nature materials*, 5(11):855–856, 2006.
- [11] Rainer Dumke, Zehuang Lu, John Close, Nick Robins, Antoine Weis, Manas Mukherjee, Gerhard Birkel, Christoph Hufnagel, Luigi Amico, Malcolm G Boshier, et al. Roadmap on quantum optical systems. *Journal of Optics*, 18(9):093001, 2016.
- [12] Philip Georgi, Marcello Massaro, Kai-Hong Luo, Basudeb Sain, Nicola Montaut, Harald Herrmann, Thomas Weiss, Guixin Li, Christine Silberhorn, and Thomas Zentgraf. Metasurface interferometry toward quantum sensors. *Light: Science & Applications*, 8(1):70, 2019.
- [13] Dong-Yeop Na, Jie Zhu, Weng C Chew, and Fernando L Teixeira. Quantum information preserving computational electromagnetics. *Physical Review A*, 102(1):013711, 2020.
- [14] Weng Cho Chew, Boyuan Zhang, and Jie Zhu. Some selected unsolved problems in classical and quantum electromagnetics. *Progress In Electromagnetics Research*, 180, 2024.
- [15] Marco Lanzagorta. *Quantum radar*. Morgan & Claypool Publishers, 2011.

- [16] I Peshko, D Mogilevtsev, I Karuseichyk, A Mikhalychev, AP Nizovtsev, G Ya Slepyan, and A Boag. Quantum noise radar: superresolution with quantum antennas by accessing spatiotemporal correlations. *Optics Express*, 27(20):29217–29231, 2019.
- [17] Patrizia Livreri, Bernardo Galvano, Luca Fasolo, Luca Oberto, Emanuele Enrico, et al. Josephson traveling wave parametric amplifier as quantum source of entangled photons for microwave quantum radar applications. *ELECTROMAGNETIC WAVES*, 179:113–124, 2024.
- [18] Gregory Ya Slepyan, Svetlana Vlasenko, and Dmitri Mogilevtsev. Quantum antennas. *Advanced Quantum Technologies*, 3(4):1900120, 2020.
- [19] Girish S Agarwal. *Quantum optics*. Cambridge University Press, 2012.
- [20] Ulf Leonhardt. Quantum physics of simple optical instruments. *Reports on Progress in Physics*, 66(7):1207, 2003.
- [21] Claude Fabre and Nicolas Treps. Modes and states in quantum optics. *Reviews of Modern Physics*, 92(3):035005, 2020.
- [22] Gregory Ya Slepyan, Dmitri Mogilevtsev, Ilay Levie, and Amir Boag. Modeling of multimodal scattering by conducting bodies in quantum optics: The method of characteristic modes. *Physical Review Applied*, 18(1):014024, 2022.
- [23] Weng Cho Chew. Quantum mechanics made simple: Lecture notes, 2012.
- [24] David AB Miller. *Quantum mechanics for scientists and engineers*. Cambridge University Press, 2008.
- [25] Kurt Gottfried. *Quantum mechanics: fundamentals*. CRC Press, 2018.
- [26] Ohad Lib and Yaron Bromberg. Quantum light in complex media and its applications. *Nature Physics*, 18(9):986–993, 2022.
- [27] Chong-Ki Hong, Zhe-Yu Ou, and Leonard Mandel. Measurement of subpicosecond time intervals between two photons by interference. *Physical review letters*, 59(18):2044, 1987.
- [28] Sudhakar Prasad, Marlan O Scully, and Werner Martienssen. A quantum description of the beam splitter. *Optics communications*, 62(3):139–145, 1987.
- [29] David Dzsojtjan, Benjamin Rousseaux, Hans R Jauslin, G Colas des Francs, Christophe Couteau, and Stéphane Guerin. Mode-selective quantization and multimodal effective models for spherically layered systems. *Physical Review A*, 94(2):023818, 2016.
- [30] R Gutiérrez-Jáuregui and R Jáuregui. Photons in the presence of parabolic mirrors. *Physical Review A*, 98(4):043808, 2018.
- [31] Patrick Maurer, Carlos Gonzalez-Ballester, and Oriol Romero-Isart. Quantum electrodynamics with a nonmoving dielectric sphere: quantizing lorenz–mie scattering. *Journal of the Optical Society of America B*, 40(12):3137–3155, 2023.
- [32] Ho Trung Dung, Ludwig Knöll, and Dirk-Gunnar Welsch. Three-dimensional quantization of the electromagnetic field in dispersive and absorbing inhomogeneous dielectrics. *Physical Review A*, 57(5):3931, 1998.
- [33] Lukas Novotny and Bert Hecht. *Principles of nano-optics*. Cambridge university press, 2012.
- [34] Stefan Scheel, Stefan Yoshi Buhmann, et al. Macroscopic quantum electrodynamics-concepts and applications. *Acta Phys. Slovaca*, 58(5):675–809, 2008.
- [35] Robert Bennett, Thomas M Barlow, and Almut Beige. A physically motivated quantization of the electromagnetic field. *European Journal of Physics*, 37(1):014001, 2015.
- [36] George W Hanson. Aspects of quantum electrodynamics compared to the classical case: Similarity and disparity of quantum and classical electromagnetics. *IEEE Antennas and Propagation Magazine*, 62(4):16–26, 2020.
- [37] Dong-Yeop Na and Weng Cho Chew. Quantum electromagnetic finite-difference time-domain solver. *Quantum Reports*, 2(2):253–265, 2020.
- [38] Salvatore Savasta, Omar Di Stefano, and Raffaello Girlanda. Light quantization for arbitrary scattering systems. *Physical Review A*, 65(4):043801, 2002.
- [39] Kane Yee. Numerical solution of initial boundary value problems involving maxwell’s equations in isotropic media. *IEEE Transactions on antennas and propagation*, 14(3):302–307, 1966.
- [40] Jian-Ming Jin. *The finite element method in electromagnetics*. John Wiley & Sons, 2015.
- [41] Allen Taflove and S. Hagness. *Computational electrodynamics: the finite-difference time-domain method*. 2nd ed, volume 67–106. 2nd ed. Norwood, 06 2000.

- [42] RJ Garbacz. Modal expansions for resonance scattering phenomena. *Proceedings of the IEEE*, 53(8):856–864, 2005.
- [43] Robert Garbacz and R Turpin. A generalized expansion for radiated and scattered fields. *IEEE transactions on Antennas and Propagation*, 19(3):348–358, 2003.
- [44] R Garbacz and D Pozar. Antenna shape synthesis using characteristic modes. *IEEE Transactions on Antennas and Propagation*, 30(3):340–350, 2003.
- [45] R Harrington and J Mautz. Theory of characteristic modes for conducting bodies. *IEEE transactions on antennas and propagation*, 19(5):622–628, 1971.
- [46] Yikai Chen and Chao-Fu Wang. *Characteristic modes: Theory and applications in antenna engineering*. John Wiley & Sons, 2015.
- [47] R Harrington and J Mautz. Computation of characteristic modes for conducting bodies. *IEEE Transactions on Antennas and Propagation*, 19(5):629–639, 2003.
- [48] Antoine Canaguier-Durand and Rémi Carminati. Quantum coherence of light emitted by two single-photon sources in a structured environment. *Physical Review A*, 93(3):033836, 2016.
- [49] Chengnian Huang and EI Wei. A parallel block preconditioner-based vie-fft algorithm for modeling the electromagnetic response from nanostructures. *IEEE Transactions on Antennas and Propagation*, 72(1):1051–1056, 2023.
- [50] Leonard Mandel and Emil Wolf. *Optical coherence and quantum optics*. Cambridge university press, 1995.
- [51] R Hanbury Brown, Richard Quinton Twiss, and givenName surName. Interferometry of the intensity fluctuations in light-i. basic theory: the correlation between photons in coherent beams of radiation. *Proceedings of the Royal Society of London. Series A. Mathematical and Physical Sciences*, 242(1230):300–324, 1957.
- [52] Roy J Glauber. The quantum theory of optical coherence. *Physical Review*, 130(6):2529, 1963.
- [53] H Jeff Kimble, Mario Dagenais, and Leonard Mandel. Photon antibunching in resonance fluorescence. *Physical Review Letters*, 39(11):691, 1977.
- [54] Gaetan Messin, Jean-Pierre Hermier, Elisabeth Giacobino, Pierre Desbiolles, and Maxime Dahan. Bunching and antibunching in the fluorescence of semiconductor nanocrystals. *Optics Letters*, 26(23):1891–1893, 2001.
- [55] Rémi Carminati, Gabriel Cwilich, Luis S Froufe-Pérez, and JJ Sáenz. Speckle fluctuations resolve the interdistance between incoherent point sources in complex media. *Physical Review A*, 91(2):023807, 2015.
- [56] Henk A Van der Vorst. Bi-cgstab: A fast and smoothly converging variant of bi-cg for the solution of nonsymmetric linear systems. *SIAM Journal on scientific and Statistical Computing*, 13(2):631–644, 1992.
- [57] Mohammadreza Khorasaninejad, Wei Ting Chen, Robert C Devlin, Jaewon Oh, Alexander Y Zhu, and Federico Capasso. Metalenses at visible wavelengths: Diffraction-limited focusing and subwavelength resolution imaging. *Science*, 352(6290):1190–1194, 2016.
- [58] Shuming Wang, Pin Chieh Wu, Vin-Cent Su, Yi-Chieh Lai, Mu-Ku Chen, Hsin Yu Kuo, Bo Han Chen, Yu Han Chen, Tzu-Ting Huang, Jung-Hsi Wang, et al. A broadband achromatic metalens in the visible. *Nature nanotechnology*, 13(3):227–232, 2018.
- [59] Lingling Huang, Xianzhong Chen, Holger Mühlenbernd, Hao Zhang, Shumei Chen, Benfeng Bai, Qiaofeng Tan, Guofan Jin, Kok-Wai Cheah, Cheng-Wei Qiu, et al. Three-dimensional optical holography using a plasmonic metasurface. *Nature communications*, 4(1):2808, 2013.